Fast-ion orbit sensitivity of neutron and gamma-ray diagnostics for one-step fusion reactions

Järleblad, H.; Stagner, L.; Salewski, M.; Eriksson, J.; Nocente, M.; Rasmussen, J.; Štancar; Kazakov, Ye O.; Simmendefeldt, B.

Published in:
Nuclear Fusion

Link to article, DOI:
10.1088/1741-4326/ac63d3

Publication date:
2022

Document Version
Peer reviewed version

Fast-ion Orbit Sensitivity of Neutron and Gamma-ray Diagnostics for One-step Fusion Reactions

H. Järleblad[1], L. Stagner[2], M. Salewski[1], J. Eriksson[3], M. Nocente[4], J. Rasmussen[1], Ž. Štancar[5,6], Ye.O. Kazakov[7], B.S. Schmidt[1] and JET Contributors*

[1] Department of Physics, Technical University of Denmark, DK-2800 Kgs. Lyngby, Denmark
[2] General Atomics, P.O. Box 85608, San Diego, California 92186-5608, USA
[3] Department of Physics and Astronomy, Uppsala University, 751 20 Uppsala, Sweden
[4] Department of Physics, University of Milano-Bicocca, 20126 Milano, Italy
[5] Jožef Stefan Institute, 1000 Ljubljana, Slovenia
[6] UKAEA, Culham Centre for Fusion Energy, Abingdon, Oxfordshire, OX14 3DB, UK
[7] Laboratory for Plasma Physics, LPP-ERM/KMS, TEC Partner, 1000 Brussels, Belgium

E-mail: `henrikj@dtu.dk`

December 2021

Abstract. Fast ions in the MeV-range can be diagnosed by neutron emission spectroscopy (NES) and gamma-ray spectroscopy (GRS). In this work, we present orbit weight functions for one-step fusion reactions, using NES and GRS diagnostics on perpendicular and oblique lines-of-sight (LOS) at JET as examples. The orbit weight functions allow us to express the sensitivities of the diagnostics in terms of fast-ion orbits and can be used to swiftly reproduce synthetic signals that have been computed by established codes. For diagnostically relevant neutron energies for the D(D,n)^{3}He reaction, the orbit sensitivities of the NES diagnostics follow a predictable pattern. As the neutron energy of interest increases, the pattern shifts upwards in fast-ion energy. For the GRS diagnostic and the T(p,γ)^{4}He reaction, the orbit sensitivity is shown to be qualitatively different for red-shifted, blue-shifted and nominal gamma birth energies. Finally, we demonstrate how orbit weight functions can be used to decompose diagnostic signals into the contributions from different orbit types. For a TRANSP simulation of the JET discharge (a three-ion ICRF scenario) considered in this work, the NES signals for both the perpendicular and oblique LOS are shown to originate mostly from co-passing orbits. In addition, a significant fraction of the NES signal for the oblique LOS is shown to originate from stagnation orbits.

* See the author list of [1].

1. Introduction

In future fusion reactors and experiments, fast ions will play a vital role in maintaining the self-sustained heating of burning plasmas [2]. However, the interaction of fast ions with the fusion plasma may lead to unstable magnetohydrodynamic (MHD) mode growth [3–5]. Fast ions can also be subject to anomalous transport [3] and be lost from the plasma [6], which may lead to a reduced heating efficiency and damage to first-wall components [7]. An understanding of the coupling between fast ions and the background plasma is therefore seen as imperative for the success of fusion energy as a viable energy source [6, 8–10].

The dynamics of fast ions is determined by the fast-ion (FI) distribution function in phase-space, which consists of position- and velocity-space. With velocity-space tomography [11–18], the velocity-space FI distribution function can be reconstructed from measurements by using the velocity-space sensitivity of the diagnostics. This sensitivity can be expressed in the form of two-dimensional weight functions. Velocity-space weight functions have been developed for numerous FI diagnostics: fast-ion D-α spectroscopy (FIDA) [19, 20], collective Thomson scattering [21], one-step [22] and two-step [23] gamma-ray spectroscopy (GRS), FI loss detectors [24, 25], neutral particle analyzers (NPA) [26], neutron emission spectroscopy (NES) [27, 28] as well as 1D weight functions for ion cyclotron emission diagnostics [29]. However, velocity-space weight functions only map the phase-space sensitivity at a single point in position space. Hence, the FI distribution function can only be reconstructed in a small measurement volume at one major radius position R and vertical position z. Orbit weight functions overcome this limitation by using the known physical relationship between the points along charged particle orbits to link isolated (R, z) points to each other. Assuming magnetic equilibrium [30], toroidal symmetry, a guiding-centre picture and low collisionality ($\nu\tau_\mathrm{p} \ll 1$ where ν is the ion-ion collisional frequency and τ_p is the orbit poloidal transit time), the complete FI distribution function can be reconstructed in terms of orbits [31], which can then be transformed into a distribution in energy E and pitch $p = v_{||}/v$ for all R and z. Orbit weight functions have so far been developed for neutron scintillators [32], NPA [32], FIDA [32] and NES [33].

In this work, we map out how the orbit sensitivity of NES [34] and GRS [35] diagnostics vary with FI- and fusion product energy (detected by the diagnostic). We examine the orbit weight functions in detail for several fusion-product energies using a perpendicular and an oblique line-of-sight (LOS) as examples, as relevant for e.g. the time-of-flight diagnostic TOFOR [36], a $LaBr_3$ detector [37, 38] and an NE213-scintillator [39] diagnostic at the Joint European Torus (JET) [1]. However, the methods developed in this work can be used to compute orbit weight functions for any diagnostic sightline and one-step fusion reaction with a neutron or gamma-photon product. The more complicated two-step fusion reactions are deferred to future work since these would require a reformulation of the methods presented in this work via the treatment of random variables [23]. Furthermore, we demonstrate that the weight functions are able to reproduce the forward model that predicts the diagnostic energy spectrum for a given fusion reaction. Lastly, the orbit weight functions are combined with FI distribution functions to analyze diagnostic signals in terms of their orbit-type constituents.

The paper is organized as follows. In section 2, orbit space and its various topological regions are introduced and the dependence on energy is explained. In section 3, we discuss the formalism behind orbit weight functions and how they can be used to rapidly compute synthetic diagnostic signals. Orbit weight functions are presented and discussed for a perpendicular sightline in section 4 (relevant for TOFOR [36] and the $LaBr_3$ GRS diagnostic [37, 38]) and for an oblique sightline in section 5 (relevant for the NE213-scintillator [39]). In section 6, orbit weight functions are used to split synthetic signals into their orbit-type constituents as well as to examine from where in orbit space the signal can be expected to originate. Lastly, a conclusion is presented in section 7.

2. Orbit space $(E, p_\mathrm{m}, R_\mathrm{m})$, including the MeV range

The full six-dimensional charged particle motion in space $\mathbf{x}$ and velocity $\mathbf{v}$ can be dimensionally reduced under relevant assumptions. If we assume toroidal symmetry, we can reduce the number of spatial dimensions by one. Similarly, by assuming the variation of the magnetic field to be negligible on the scale of the gyro-motion of the ion, so that the gyro-motion is approximately a rotation around a circle, we can reduce the number of velocity dimensions by one. If we also assume the motion of the ion to have been unperturbed as it revisits the same (R, z) coordinate, we can uniquely label all charged particle trajectories in a magnetic equilibrium with just one spatial coordinate and two velocity coordinates. Given these assumptions, the particle motion is periodic and follows fixed spatial trajectories called orbits. Since our aim is to ultimately utilize three-dimensional orbit phase space for tomographic inversion, the coordinates should be chosen carefully. It is arguably preferable to choose the coordinates so that the space has

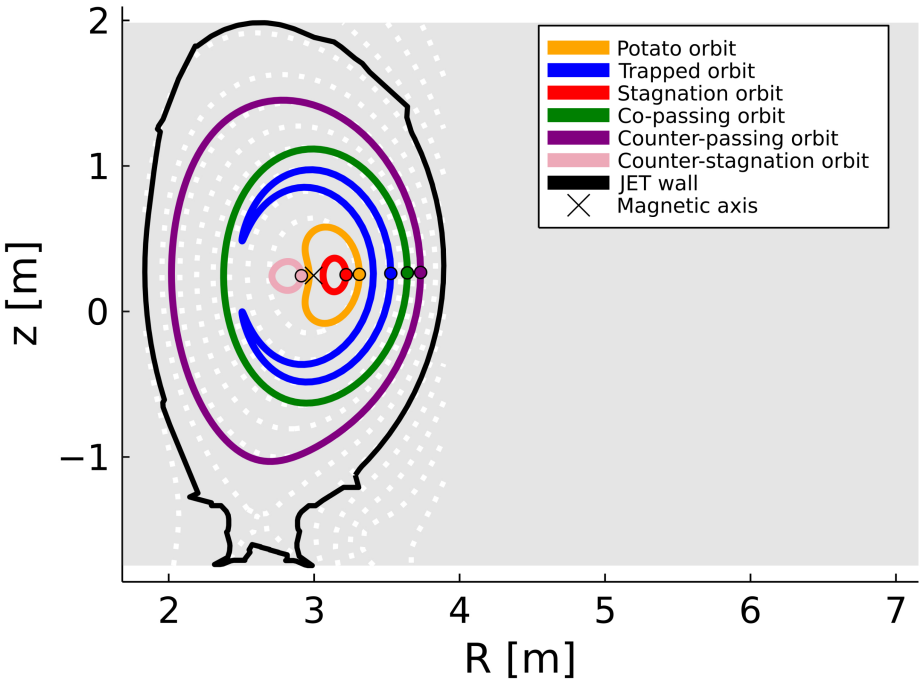

Figure 1. Example (deuterium) orbits with $(E[\mathrm{keV}], p_\mathrm{m}[-], R_\mathrm{m}[\mathrm{m}])$-coordinates $(412.6, 0.333, 3.31)$ (potato), $(69.9, 0.535, 3.53)$ (trapped), $(2125.9, 0.333, 3.22)$ (stagnation), $(481.1, 0.758, 3.64)$ (co-passing), $(138.5, -0.980, 3.73)$ (counter-passing) and $(2262.9, -0.333, 2.91)$ (counter-stagnation) for JET shot No. 94701 at 10.79 s. The colored lines show the poloidal projections of the guiding-center trajectories. the dotted white lines correspond to the magnetic flux surfaces. The colored points mark the R_m-coordinates of the orbits.

clear, finite boundaries and does not mix position and velocity space [40]. Therefore, in this work, we use the $(E, p_\mathrm{m}, R_\mathrm{m})$ orbit-space coordinates [32]. E is the kinetic energy of the particle, and p_m is the pitch $(v_{||}/v)$ at the maximum major radius position R_m of (the guiding-center of) the orbit. All possible orbits in a given tokamak equilibrium can be uniquely identified with an $(E, p_\mathrm{m}, R_\mathrm{m})$ triplet. For a given FI energy E, orbit space is bounded by $[-1, 1]$ in p_m and $[R_\mathrm{axis} - \delta R, R_\mathrm{LFS}]$ in R_m, where R_axis and R_LFS are the major radius positions of the magnetic axis and the low-field side wall, respectively. δR can vary but has a natural maximum of $\delta R = R_\mathrm{axis} - R_\mathrm{HFS}$ where R_HFS is the location of the high-field side wall. However, in practice, $\delta R = 1/5(R_\mathrm{axis} - R_\mathrm{HFS})$ is usually enough to include all possible populatable orbits when working with orbit space.

In this work, all orbit-space quantities have been computed assuming the magnetic equilibrium of JET shot No. 94701 at 10.79 s [35, 41–43], a three-ion ICRF scheme with core-localized FI generation. Examples of the different orbit types and their corresponding $(E, p_\mathrm{m}, R_\mathrm{m})$ coordinates are shown in Figure 1.

Together, the three coordinates span a three-dimensional space, named orbit space, where every point corresponds to a unique orbit. As can be seen in Figure 2, orbit space can be divided into different topological regions where every region corresponds to a specific orbit type. The exact shape, position and size of a topological region depend on the magnetic equilibrium, particle species and FI energy. Near thermal energies of a few keV, there are primarily three regions of appreciable size: co-passing, trapped and counter-passing. At higher energies, three additional regions grow to significant size: potato, stagnation and counter-stagnation. At the same time, the trapped, co- and counter-passing regions shrink. This means that at progressively higher FI energies, an increasing fraction of the populatable orbits will be potato, stagnation and counter-stagnation orbits. This is relevant for fusion-born ions (such as DT-born alpha particles (3.52 MeV), DD-born protons (3.02 MeV) and ^{3}He ions (0.82 MeV), and D^{3}He-born protons (14.7 MeV) [44]). Furthermore, a large portion of orbit space will contain invalid and lost orbits (gray and brown regions in Figure 2, respectively). Invalid orbits are orbits whose $(E, p_\mathrm{m}, R_\mathrm{m})$ coordinates correspond to unrealizable particle trajectories given the magnetic equilibrium. Lost orbits are orbits with trajectories that intersect the tokamak wall. The lost region also grows at increasingly high FI energies.

Lastly, the orbit-space topology depends on the particle species and magnetic equilibrium. This can be understood from the Lorentz force law $m\mathbf{a} = q(\mathbf{E} +$

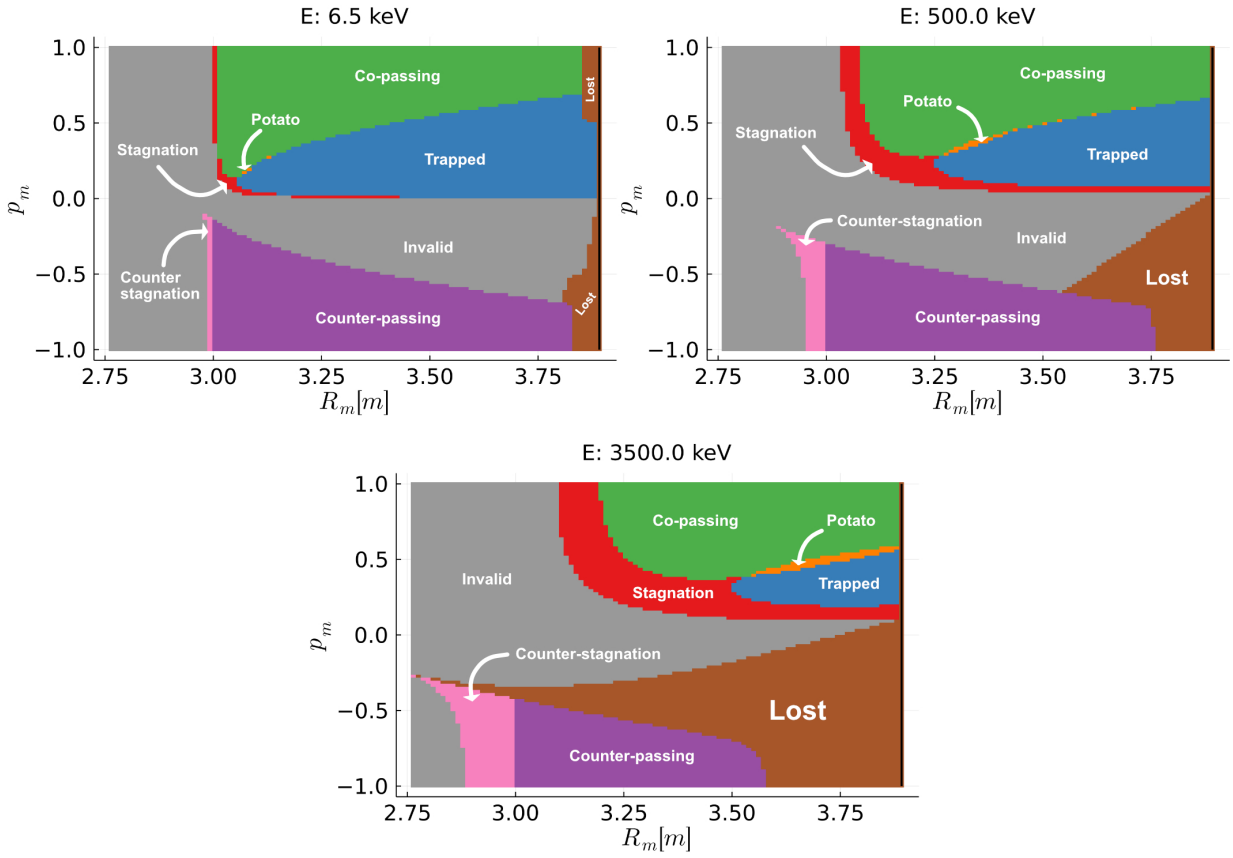

Figure 2. Orbit-space topology for JET shot No. 94701 at 10.79 s for three energy slices (FI energy held constant). The black line marks the JET low-field side wall. The topology was computed for deuterium ions. 6.5 keV is the temperature of the bulk ion distribution at the magnetic axis. 500 keV and 3500 keV were chosen to illustrate the energy dependence of the orbit-space topology.

$\mathbf{v} \times \mathbf{B}$) which determines the particle acceleration and hence trajectory.

3. Weight function formalism

To derive the phase-space sensitivity of diagnostics, consider a fast ion with position coordinate $\mathbf{x}$ and velocity coordinate $\mathbf{v}$. A weight function can be viewed as a mapping between a general FI distribution $f(\mathbf{x}, \mathbf{v})$ and the resulting diagnostic signal s via the following relation [19, 20, 45]:

$$s(E_{1,\mathrm{d}}, E_{2,\mathrm{d}}) = \int w(E_{1,\mathrm{d}}, E_{2,\mathrm{d}}, \mathbf{x}, \mathbf{v}) f(\mathbf{x}, \mathbf{v}) \mathrm{d}\mathbf{x}\mathrm{d}\mathbf{v} \quad (1)$$

where $E_{1,\mathrm{d}}$ and $E_{2,\mathrm{d}}$ mark the lower and upper boundaries of a diagnostic energy bin and $w(E_{1,\mathrm{d}}, E_{2,\mathrm{d}}, \mathbf{x}, \mathbf{v})$ is the weight function. Both the signal and the weight function will thus depend on the diagnostic energy bin for which the measurement is considered. Equation (1) can then be written specifically for our $(E, p_\mathrm{m}, R_\mathrm{m})$ orbit space as follows

$$s(E_{1,\mathrm{d}}, E_{2,\mathrm{d}}) = \int w(E_{1,\mathrm{d}}, E_{2,\mathrm{d}}, E, p_\mathrm{m}, R_\mathrm{m}) f(E, p_\mathrm{m}, R_\mathrm{m}) \mathrm{d}E \mathrm{d}p_\mathrm{m} \mathrm{d}R_\mathrm{m}. \quad (2)$$

Here, we have assumed toroidal symmetry, a guiding-centre picture and low collisionality as explained in Section 1. Equation (2) can then be discretized to give

$$s(E_{1,\mathrm{d}}, E_{2,\mathrm{d}}) = \sum_{i,j,k} w(E_{1,\mathrm{d}}, E_{2,\mathrm{d}}, E_i, p_{\mathrm{m},j}, R_{\mathrm{m},k}) f(E_i, p_{\mathrm{m},j}, R_{\mathrm{m},k}) \Delta E \Delta p_\mathrm{m} \Delta R_\mathrm{m}. \quad (3)$$

To get a practical relationship between the signal of a diagnostic, which consists of several energy bins, and the FI orbit-space distribution, we write the matrix equation

$$S = WF \quad (4)$$

where S has the size *number of diagnostic energy bins* $\times$ 1, W has the size *number of diagnostic energy bins* $\times$ *number of valid orbits* and F has the size *number of valid orbits* $\times$ 1. The factor $\Delta E \Delta p_\mathrm{m} \Delta R_\mathrm{m}$ has been absorbed into W. We have thus vectorized our orbit-space quantities and stacked the weight functions row by row into a matrix. Hence, every row of equation (4) is a case of equation (3). Equation (4) is mathematically the same equation as is used for velocity-space tomography (and position-space tomography).

At this point, it can be helpful to introduce and explain some nomenclature. In the context of orbit space,

- *a weight* relates a single diagnostic energy bin to a single $(E, p_\mathrm{m}, R_\mathrm{m})$ grid point. For a specific diagnostic energy bin $(E_{1,\mathrm{d}}, E_{2,\mathrm{d}})$, it describes the sensitivity of the diagnostic to the orbit at that particular orbit-space grid point. It has the dimensions of *signal per ion* (the dimensions of the signal depend on what diagnostic is used).
- *a weight function* relates a single diagnostic energy bin to all points in orbit space. A discretized weight function is thus comprised of many individual weights. It is a function of the three orbit-space coordinates as $w(E, p_\mathrm{m}, R_\mathrm{m})$.
- *a weight function matrix* (or weight matrix for short) is a matrix where each row is a vectorized discretized weight function. Each row corresponds to a specific diagnostic energy bin and each column corresponds to a particular orbit.

From here on, the label 'discretized' will be omitted for brevity.

3.1. Computing weight matrices and orbit weight functions

To compute a weight matrix, the forward model of the diagnostic is used to compute predicted signals for all valid orbits of a particular orbit grid. A set of diagnostic energy bins of interest ($[E_{1,\mathrm{d}}, E_{2,\mathrm{d}}$),$[E_{2,\mathrm{d}}, E_{3,\mathrm{d}}$),...,$[E_{n-1,\mathrm{d}}, E_{n,\mathrm{d}}]$), reflecting the spectral resolution of the diagnostic, must be assumed for the weight matrix. Each valid orbit is assumed to be populated by only a single particle (to achieve correct normalization) and the orbit is split up into its (E, p, R, z) constituent points. Each (E, p, R, z) point is then weighted according to the fraction of the total poloidal transit time spent by the particle on a path length dl between that (E, p, R, z) point and the next. The number of (E, p, R, z) points needed to accurately represent an orbit will vary depending on the required numerical accuracy [46], the complexity of the orbit as well as the width of the (R, z)-projection of the viewing cone of the diagnostic. In this work, $\geq$ 500 points were used throughout. For one orbit, all weighted points effectively constitute an (E, p, R, z) distribution for which the expected signal can be computed with the forward model [47] for a given instrument (e.g. TOFOR). This signal represents one column in the weight matrix and the process is then repeated for all valid orbits, resulting in the complete weight matrix. Every row of the matrix then corresponds to an orbit weight function and describes the orbit-space sensitivity for a specific diagnostic energy bin.

Mathematically, this way of computing the weight functions can be understood via equation (2) and setting $f(E, p_\mathrm{m}, R_\mathrm{m}) = \delta(E - E_i)\delta(p_\mathrm{m} - p_{\mathrm{m},j})\delta(R_\mathrm{m} - R_{\mathrm{m},k})$ to model the single-particle valid orbit. We get

$$\begin{aligned} s(E_{1,\mathrm{d}}, E_{2,\mathrm{d}}) = \int & w(E_{1,\mathrm{d}}, E_{2,\mathrm{d}}, E, p_\mathrm{m}, R_\mathrm{m})\delta(E - E_i) \\ & \delta(p_\mathrm{m} - p_{\mathrm{m},j})\delta(R_\mathrm{m} - R_{\mathrm{m},k}) dE dp_\mathrm{m} dR_\mathrm{m} \\ = & w(E_{1,\mathrm{d}}, E_{2,\mathrm{d}}, E_i, p_{\mathrm{m},j}, R_{\mathrm{m},k}) \end{aligned} \tag{5}$$

where $(E_i, p_{\mathrm{m},j}, R_{\mathrm{m},k})$ denotes the orbit-space coordinate of interest. Note that equation (5) simply describes the sensitivity in orbit space but does not yet account for the extent to which these orbits are actually populated (via F). As can be understood from equation (4), for a given FI distribution F, the weight matrix W can be used to very rapidly compute the expected diagnostic signal S instead of performing the more time-consuming computations usually needed to compute synthetic signals. This is advantageous if synthetic signals for many distribution functions are to be computed.

3.2. Validating orbit weight functions

To confirm that the weight matrix is equivalent to the standard forward model, synthetic signals S (computed via the DRESS code [47] forward model) are plotted together with the 'weight matrix signals' WF for given FI distributions in Figure 3. This has been done for NES and GRS diagnostics with perpendicular sightlines (corresponding to the LOS of TOFOR [36] and a $LaBr_3$ gamma-ray detector [37, 38]) and for an additional NES diagnostic with an oblique sightline (corresponding to the LOS of a NE213-scintillator [39]). Their sightlines are illustrated in Figure 4. The $\mathrm{D(D,n)^3He}$ reaction was used for the NES diagnostics and the $\mathrm{T(p,\gamma)^4He}$ reaction was used for the GRS diagnostic.

For the NES diagnostics, the average FI deuterium distribution function was computed for JET shot No. 94701 for our time window of interest using the TRANSP [48] code (v19.2) with the NUBEAM [49] module coupled to TORIC [50] (for the RF-acceleration of the ions) together with the RF kick operator [51, 52]. The magnetic equilibrium at 10.79 s is thus used as the average magnetic equilibrium for our time window. The time traces of the neutral beam injection (NBI) and ion cyclotron resonance heating (ICRH) power are shown in Figure 5a, and the FI deuterium distribution function is plotted as a function of energy in Figure 5b (where the other dimensions have been integrated out). The thermal deuterium distribution is plotted as an inset in Figure 4.

For the GRS diagnostic, the same n_i and T_i profiles as in Figure 4 were used for the thermal tritium distribution but the n_i profile was re-normalized so

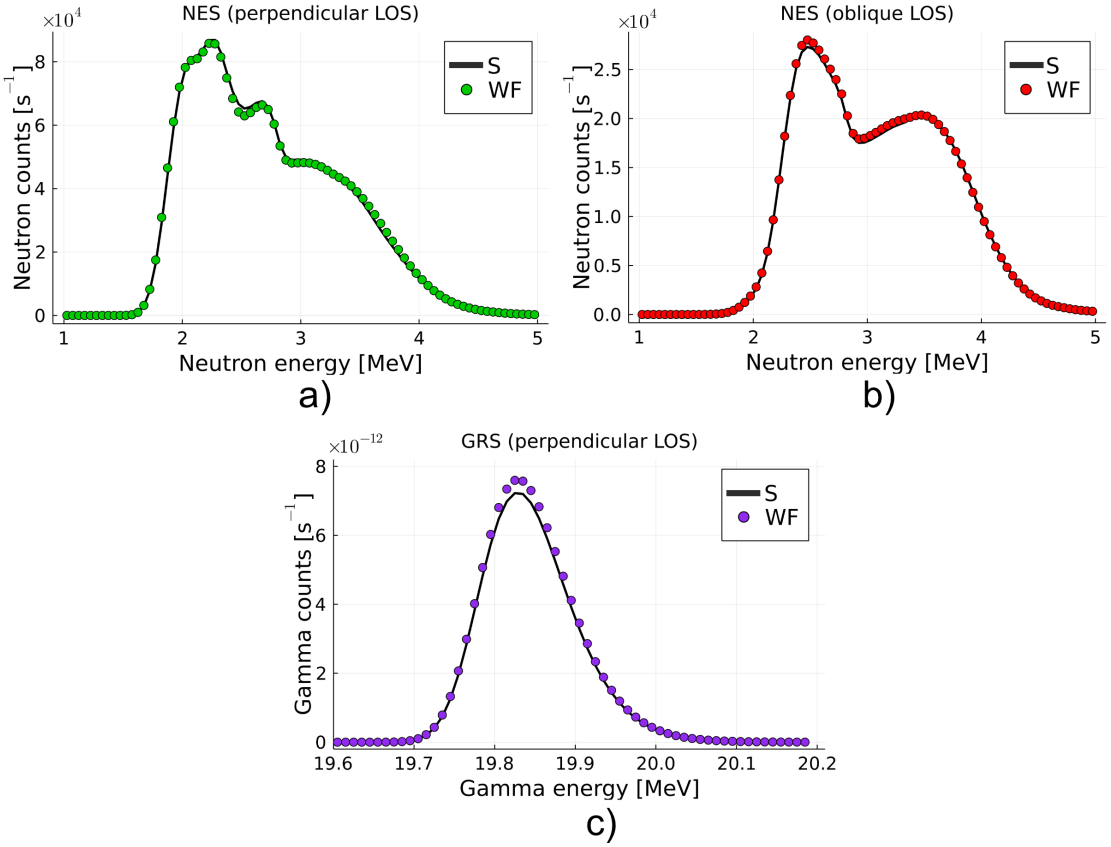

Figure 3. The predicted diagnostic signals computed via the forward model (S) and via the weight matrix (WF) for NES with a perpendicular sightline (a) and an oblique sightline (b), as well as for GRS with a perpendicular sightline (c). The NES signals are computed using the D(D,n)^{3}He reaction and the GRS signal is computed using the T(p,γ)^{4}He reaction. The NES WF signals were computed using a $2400 \times 102 \times 104$ grid in orbit space with $E = [1.4, 2400.0]$ keV, $p_{\mathrm{m}} = [-1.0, 1.0]$ and $R_{\mathrm{m}} = [2.76, 3.89]$ m. The GRS WF signal was computed using the same grid points in p_{m} and R_{m} but with 600 grid points in fast-ion energy E and $E = [1.4, 600.0]$ keV. Please note that this relatively high orbit-space grid resolution was only used in order to validate that the WF and S signals converge as grid resolution increases.

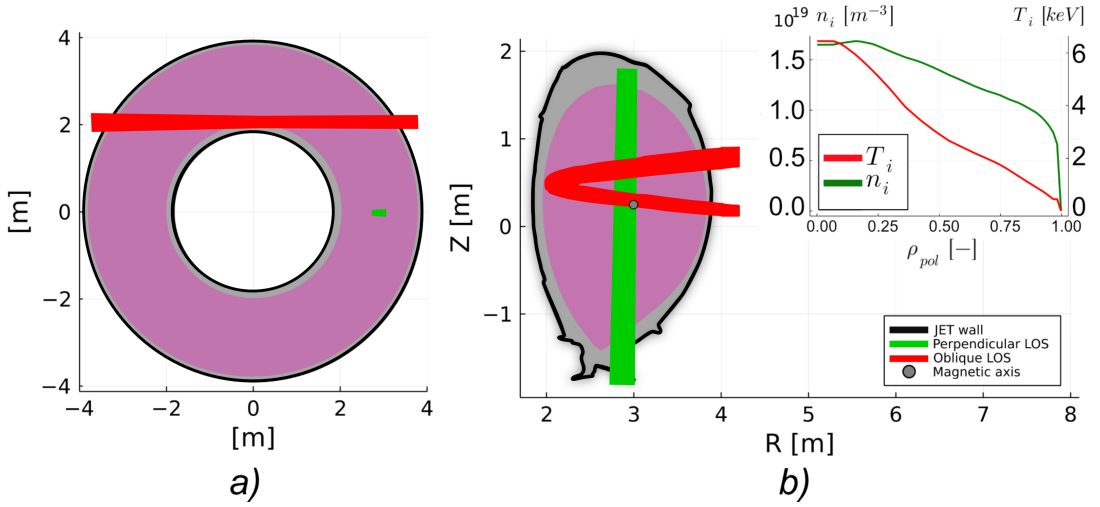

Figure 4. The viewing cones of the perpendicular (green) and oblique (red) sightlines, projected onto a toroidal (a) and poloidal (b) view. The plasma within the last closed flux surface (LCFS) is depicted in indigo. The bulk (deuterium) density n_{i} and temperature T_{i} profiles for JET shot No. 94701, averaged over our time window of interest, are shown as an inset. The electron density n_{e} and temperature T_{e} were measured with High Resolution Thomson Scattering, after which $T_{\mathrm{i}} = T_{\mathrm{e}}$ was assumed. n_{i} was estimated from n_{e} together with measurements of Z_{eff} made by Visible Bremsstrahlung diagnostics and the assumption that impurity ions are exclusively Beryllium. The n_{i} and T_{i} profiles correspond to data between R_{axis} and R_{LCFS} at z_{axis} and are representative for the plasma as a whole.

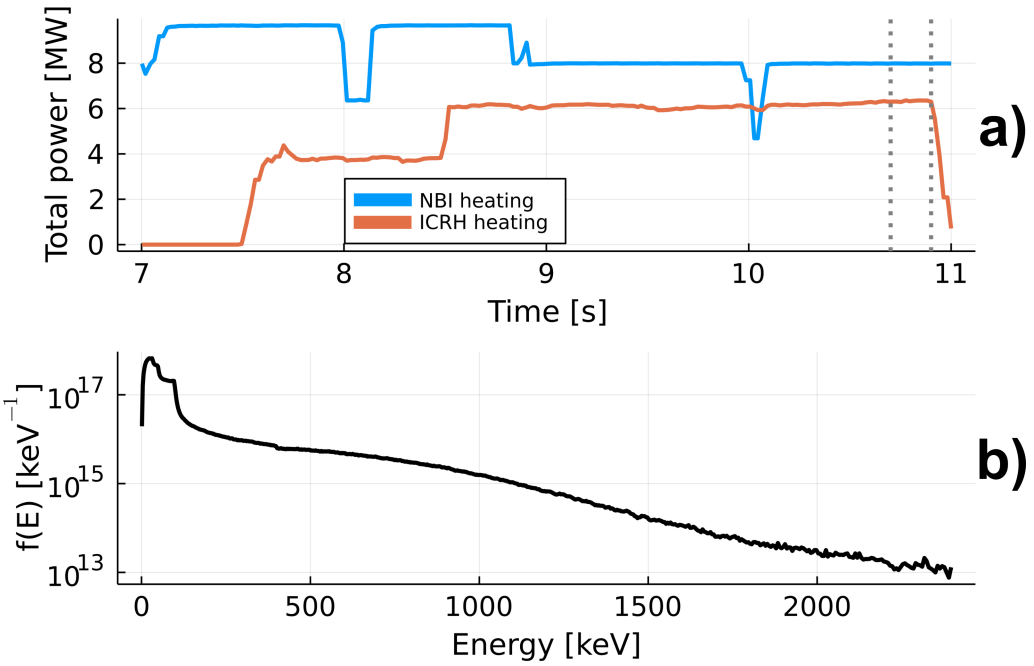

Figure 5. The total injected NBI and ICRH power as functions of time for JET shot No. 94701 are shown in a). The dotted lines delimit the time window of this work. The corresponding average TRANSP NUBEAM-computed FI deuterium distribution function for the time window is shown in b) as a function of energy.

that $n_{\mathrm{T}} = 10^{13}$ m^{-3} on-axis. For the fast protons, a Maxwellian distribution was used with $T = 30$ keV and with the same 2D (R, z) density profile as that of the TRANSP FI deuterium distribution used in this work. The total number of fast protons was set to $N_{\mathrm{p}} = 6 \times 10^{13}$.

As we can observe from Figure 3, the signals produced by multiplying the orbit weight functions (W) with the FI distribution functions (F) closely match the signals computed via the conventional forward model (S). This confirms that the orbit weight functions are computed correctly and provide an accurate map of the orbit-space sensitivity of the diagnostics, which we will examine in sections 4 and 5.

4. Orbit Weight Functions for Perpendicular Sightlines

4.1. Neutron emission spectroscopy

Based on the formalism in sections 2 and 3, Figure 6 shows examples of the orbit sensitivity of the perpendicular sightline at JET (the sightline of TOFOR) for selected FI energies E and diagnostic (neutron) energies E_{d}. For each diagnostic energy of an NES (or GRS) spectrum, we will show three selected slices of the corresponding 3D orbit weight function. The orbit sensitivity displays a complicated dependence on the orbit-space coordinates and diagnostic (here neutron) energy E_{d}. Nevertheless, certain general features can be identified. For all three neutron energies, the orbit sensitivity is relatively concentrated around the potato region (Figure 6 aa, ba and ca) for the lowest E considered here and then widens outwards towards the $p_{\mathrm{m}} = \pm 1.0$ boundaries at increasing FI energies (ab-ad, bb-bd and cb-cd). For potato orbits, the ion spends a large fraction of its poloidal transit time inside the LOS and $v_{||} \to 0$ ($v_{\perp}/v \to 1$) at the same time. Ions on potato orbits are thus able to produce a large amount of up-shift of the neutron nominal birth energy (which is most important at low FI energies) for a large fraction of the poloidal transit time. This results in a relatively large orbit sensitivity for the E and E_{d} of interest (Figure 6 aa, ba and ca). Furthermore, the narrow region of relatively high sensitivity of trapped orbits (most clearly visible in Figure 6 aa-ad) is due to the 'banana tips' perfectly coinciding with the perpendicular sightline [33]. The ions spend a relatively large fraction of their poloidal transit time at these banana tips, which results in a relatively large sensitivity. At higher FI energies, the counter-stagnation region becomes the area of highest sensitivity. This is because counter-stagnation orbits have the poloidal projection of their trajectories almost completely within the perpendicular sightline. For the TRANSP FI deuterium distribution examined in this work, the counter-stagnation orbits are scarcely populated, as shown in Figure 7. However, in future fusion devices, the counter-stagnation orbits are likely

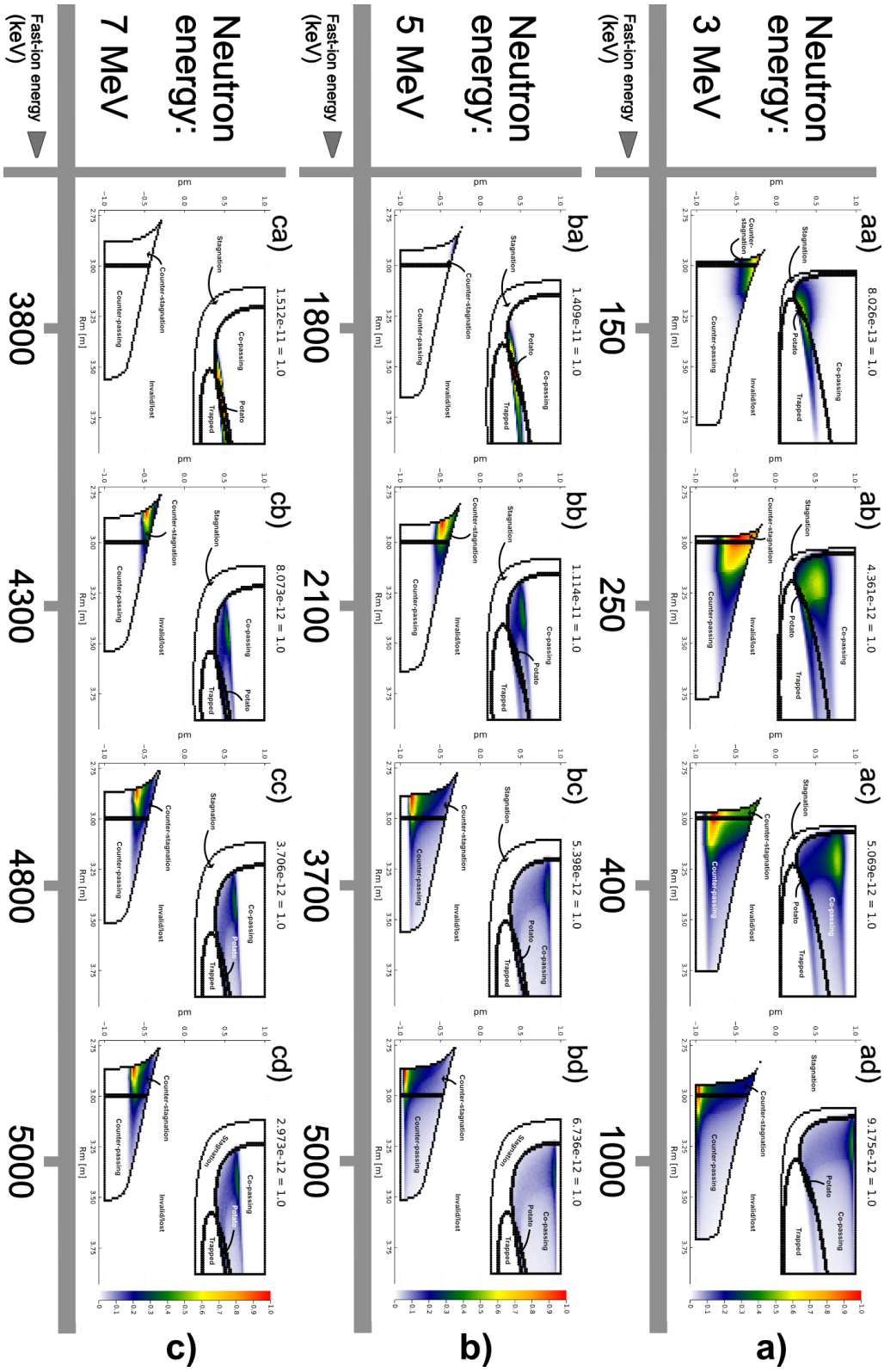

Figure 6. Three orbit weight functions for the perpendicular sightline (corresponding to the LOS of e.g. TOFOR [36]) and D(D,n)^{3}He reaction. The number of grid points in p_m and R_m is 100. The neutron energies of (a) 3, (b) 5 and (c) 7 MeV were chosen because neutron energies down-shifted below the nominal D(D,n)^{3}He birth energy of 2.45 MeV are diagnostically indistinguishable from scattered neutrons. The FI energy refers to one of the fusing deuterium ions. For ease of visualization, the data in each energy slice has been normalized to have a maximum value of 1.0. The actual maximum value $w_{E,max}$ is found in the title of each slice plot as $w_{E,max} = 1.0$.

going to be populated by fusion-born alpha particles because of their high energy and (approximately) isotropic birth pitch distribution.

As we look at increasingly higher neutron energies, the features of the weight functions stay roughly the same but the 3D structures are translated 'upwards' to higher FI energies.

4.2. Gamma-ray spectroscopy

The GRS diagnostic examined in this paper has the same sightline as the perpendicular NES diagnostic. Therefore, the NES and GRS orbit weight functions will have similar orbit sensitivity due to the usage of the same sightline, but differences due to the masslessness of the T(p,γ)^{4}He gamma photon [22]. As can be seen in Figure 8a, the orbit sensitivity for gamma energies below the nominal birth energy is relatively low (maximum $w_{E,max}$ in Figure 8a is an order of magnitude smaller than maximum $w_{E,max}$ in Figure 8b and three orders of magnitude smaller than maximum $w_{E,max}$ in Figure 8c). This is consistent with the often strongly asymmetric shape of one-step reaction GRS spectra, which have low signal levels below the nominal gamma nominal birth energy [54]. The sensitivity is mostly concentrated around the tip of the counter-stagnation region in the $p_\mathrm{m} < 0.0$ half-plane and the potato region in the $p_\mathrm{m} > 0.0$ half-plane. All weights become zero for higher FI energies (Figure 8ad). This is because fast ions with such a high energy will result in gamma photons with too high energy for the 19.7 MeV diagnostic energy bin.

At gamma energies close to the nominal birth energy, the orbit sensitivity is non-zero down to thermal ion energies and up to the several hundreds of keVs, as can be observed in Figure 8b. Just above thermal ion energies, the area of highest sensitivity tends outwards towards the $p_\mathrm{m} = \pm 1.0$ boundaries (Figure 8bb) before reverting back in towards the tip of the counter-stagnation and potato regions (Figure 8bc) at increasing E. Similar to the orbit weight function for the 19.7 MeV diagnostic energy bin, all weights become zero for sufficiently high FI energies.

At gamma energies above the nominal birth energy, the orbit sensitivity follows a predictable pattern. At relatively low FI energies (Figure 8ca), the sensitivity is mainly concentrated around the potato region and tip of the counter-stagnation region. This is similar to the orbit sensitivity for gamma energies below the nominal birth energy (Figure 8 aa-ac), but the reason is now due to the need for blue-shift instead of red-shift of the gamma birth energy. At increasing FI energy (Figure 8cb and cc) the sensitivity becomes more concentrated towards the $p_\mathrm{m} = \pm 1.0$ boundaries, but again migrates inward towards the potato region and the tip of the counter-stagnation region at $E \approx 2$ MeV (Figure 8cd). At FI energies above ≈ 2500.0 keV, all weights become zero for the 21.0 MeV diagnostic energy bin. For increasingly high gamma energy bins ($E_\mathrm{d} > 21.0$ MeV), the whole pattern observed for the 21.0 MeV orbit weight function will stay roughly the same and move 'upwards' to higher FI energies.

5. Orbit Weight Functions for an Oblique Sightline (NES)

The viewing cone of the NE213-scintillator NES diagnostic considered in this paper has an oblique sightline w.r.t. **B**. Therefore, the patterns of the weight functions will differ significantly compared to those associated with the perpendicular sightline. However, the non-zero weights will be found in similar FI- and neutron energy ranges as for the perpendicular sightline because the same fusion reaction D(D,n)^{3}He is being considered. In Figure 9, we can observe how the non-zero weights are mostly concentrated to the $p_\mathrm{m} > 0.0$ half-plane. The orbits in the $p_\mathrm{m} < 0.0$ half-plane will result in ion motion exclusively away from the oblique NES diagnostic. Ions on these orbits are therefore mostly unable to produce the up-shift required for the neutron energies of interest. However, at high FI energies, the counter-stagnation orbits have enough energy and just the right pitch as they cross the oblique sightline that they can produce sufficient up-shift as well (Figure 9 ad and bd). Furthermore, the following similar overall features can be observed in all weight functions (Figure 9 a-c). The areas of highest sensitivity are concentrated to two islands close to the stagnation region and in the middle of the co-passing region. These areas then split at increasingly high FI energies. They tend toward the $p_\mathrm{m} = 1.0$ boundary and the bottom of the stagnation region. At very high FI energies (Figure 9 ad, bd and cd), the sensitivity close to the $p_\mathrm{m} = 1.0$ boundary starts to become zero since ions on those orbits will now produce too much up-shift for the neutron energies of interest. Similar to the case of the perpendicular diagnostics, for increasingly high neutron energies the 3D pattern will stay roughly the same and move 'upwards' to higher FI energies.

6. Orbit-space Origin of Diagnostic Signals for Given FI Distribution Functions

With orbit weight functions, we can split the predicted diagnostic signal of a FI distribution function into orbit-type constituents. Mathematically, this can be expressed as

$$WF = \sum_h W_h F_h \tag{6}$$

where h labels all the different orbit types (co-passing, trapped, etc). The FI distribution function

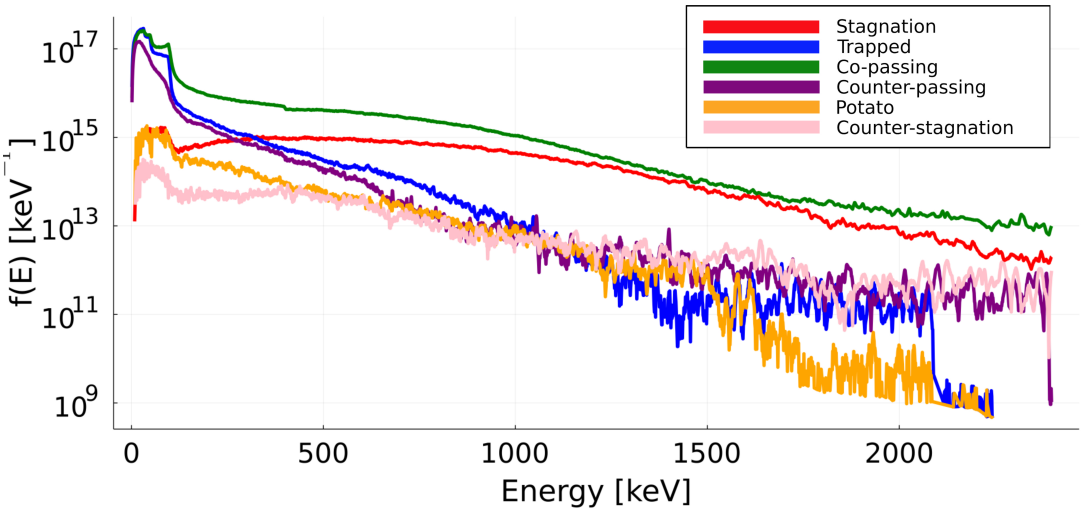

Figure 7. The same TRANSP NUBEAM-computed FI deuterium distribution function as shown in Figure 5 b), but split into its orbit-type constituents. The sum of all the colored lines equals the black line in Figure 5 b). The significant population of MeV-range co-passing fast ions for three-ion ICRF schemes at JET has been discussed in [53]. The noise at high energies is due to sampling and can be reduced if we increase the number of orbit samples when transforming the FI distribution to orbit space.

in terms of orbit types (F_h) can be obtained by transforming the FI distribution function into orbit space to obtain $f(E, p_\mathrm{m}, R_\mathrm{m})$, and identifying the $(E, p_\mathrm{m}, R_\mathrm{m})$ coordinates corresponding to a given orbit type. This is also the method which allows us to split e.g. $f(E)$ into its orbit-type constituents (as in Figure 7). Via pointwise multiplication between F_h and $w(E, p_\mathrm{m}, R_\mathrm{m})$, we can obtain signal contributions for every diagnostic energy bin in terms of orbit types. This allows us to re-examine the diagnostic signals of Figure 3 in terms of orbit types, as shown in Figure 10. For the perpendicular LOS with NES and the average FI deuterium distribution function for JET shot No. 94701 for our time window of interest, the signal comes mainly from co-passing orbits for all neutron energies of interest. At neutron energies around the nominal birth energy (2.45 MeV), there are also significant contributions from trapped and counter-passing orbits to the signal generated by fast ions. However, this neutron energy range is difficult to diagnose due to the presence of down-scattered neutrons. For the oblique LOS with NES and the same FI distribution, in addition to co-passing orbits a large portion of the signal comes from stagnation orbits. For the perpendicular LOS with GRS and the Maxwellian FI test distribution (discussed in section 3.2), the signal comes from co-passing, counter-passing and trapped orbits in comparable fractions.

By normalizing the signal to 1.0 for all neutron energies of interest (Figure 11), we can examine the signal contributions from different orbit types more closely. For the diagnostics with the perpendicular LOS (Figure 11a and c, respectively), the normalized plots confirm the deductions made from Figure 10a and Figure 10c. For the oblique LOS with NES (Figure 11b), we can observe how the contributions from all orbit types but counter-passing and counter-stagnation orbits vanish for neutron energies below 2.0 MeV. This is because heavy down-shift of the neutron nominal birth energy is required for a neutron to be detected in those diagnostic energy bins. The only orbit types that can produce that type of down-shift, given the oblique sightline, are counter-passing and counter-stagnation orbits. However, note that the absolute magnitude of the diagnostic signal starts to vanish for such heavily down-shifted neutron energies. In addition, the signal at those neutron energies is usually heavily dominated by scattered neutrons, which makes the neutron energy range unusable for diagnosing fast ions [2].

Finally, we can also examine the expected origin of the diagnostic signal in orbit space in detail. This is illustrated in Figure 12. At $E = 150$ keV, we have populated orbits of all types, and we might expect them all to contribute to the signal. However, when pointwise multiplied with an NES orbit weight function, such as the $w(150\,\mathrm{keV}, p_\mathrm{m}, R_\mathrm{m})$ for neutron energy $E_\mathrm{d} = 3$ MeV (corresponding to Figure 6aa), we can observe that almost all NES signal will originate from potato-like orbits for the neutron and FI energies of interest. This is because at $E = 150$ keV and $E_\mathrm{d} = 3$ MeV, the NES orbit weight function for the perpendicular LOS (e.g. TOFOR) is non-zero almost exclusively for potato-like orbits.

7. Conclusion

In this work, orbit weight functions have been presented for one-step fusion reactions, using a

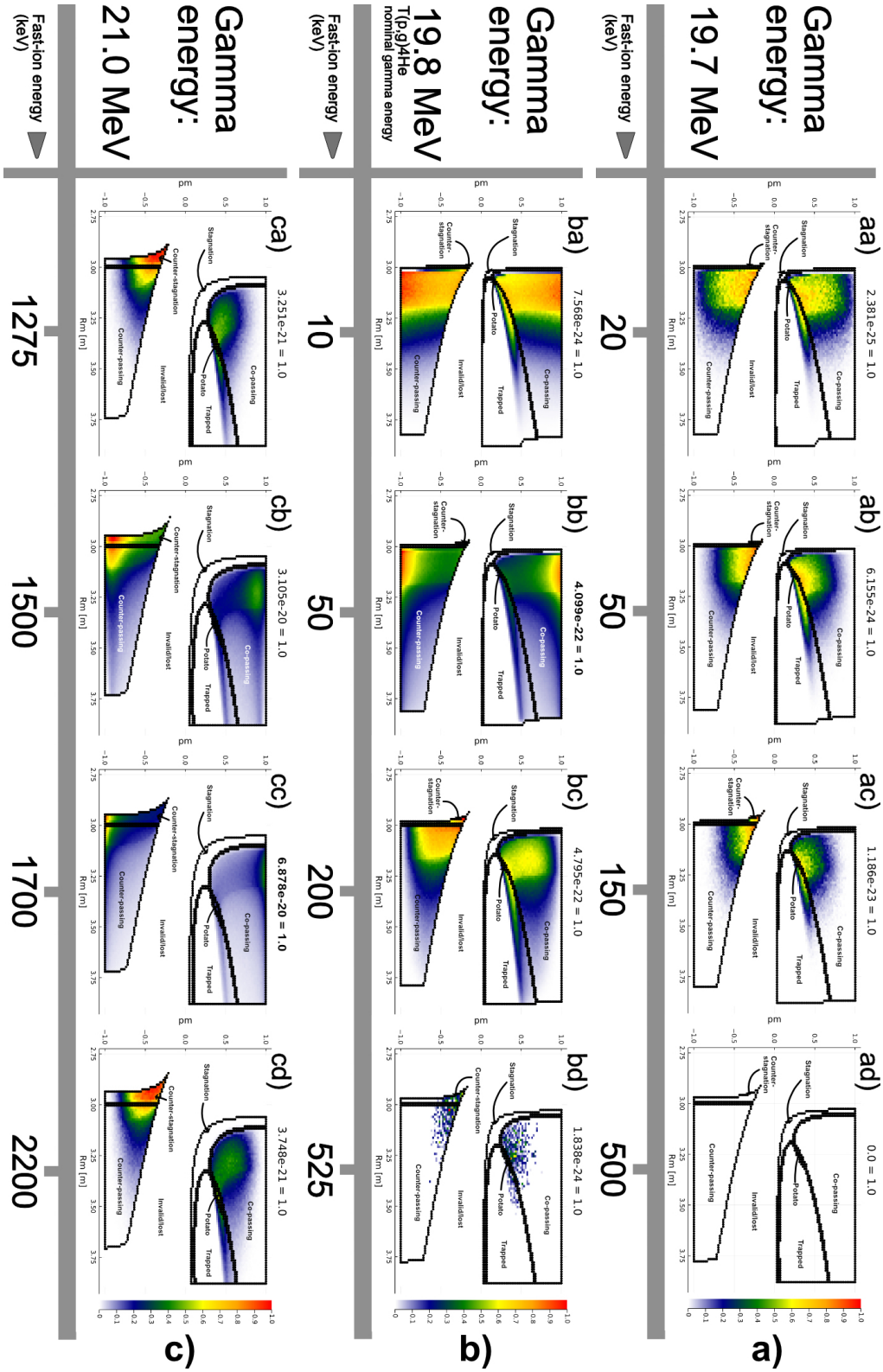

Figure 8. Three orbit weight functions for the perpendicular sightline (corresponding to the LOS of e.g. the $LaBr_3$ diagnostic [37,38]) and T(p,γ)^{4}He reaction. One at red-shifted gamma energies (a), one at the T(p,γ)^{4}He gamma nominal energy (b) and one at blue-shifted gamma energies (c). The number of grid points in p_m and R_m is 100. The FI energy refers to the proton energy of the T(p,γ)^{4}He fusion reaction. For ease of visualization, the data in each energy slice has been normalized to have a maximum value of 1.0. The actual maximum value $w_{E,max}$ is found in the title of each slice plot as $w_{E,max} = 1.0$.

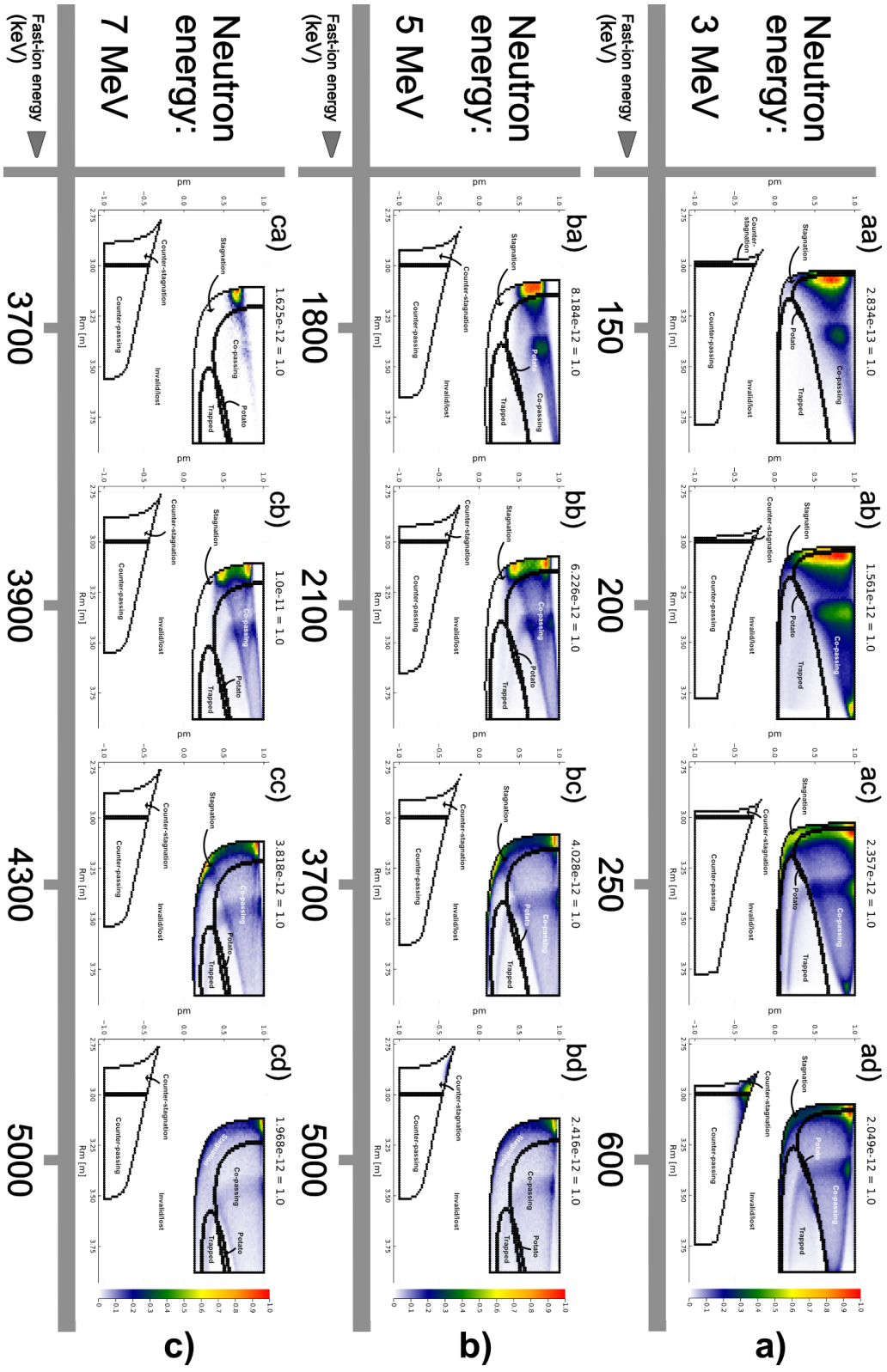

Figure 9. Three orbit weight functions for the oblique sightline (corresponding to the LOS of e.g. the NE213-scintillator diagnostic [39]) and D(D,n)^{3}He reaction. The number of grid points in p_m and R_m is 100. The FI energy refers to one of the fusing deuterium ions. For ease of visualization, the data in each energy slice has been normalized to have a maximum value of 1.0. The actual maximum value $w_{E,max}$ is found in the title of each slice plot as $w_{E,max} = 1.0$.

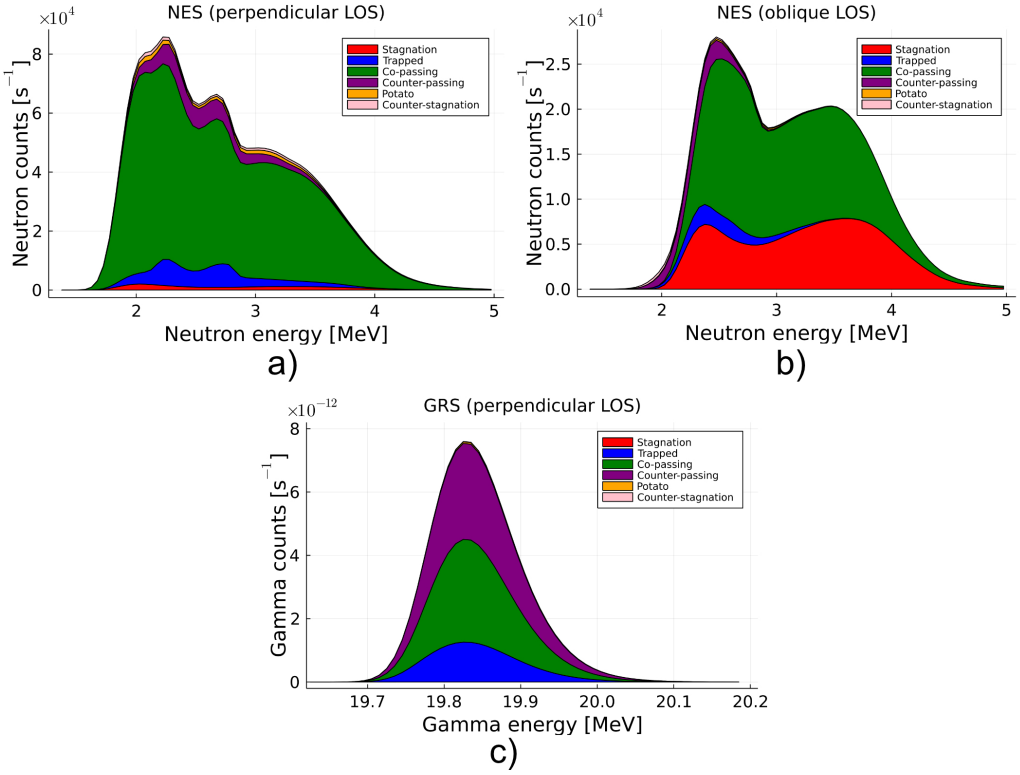

Figure 10. Diagnostic signals split into their orbit type constituents for a) NES with perpendicular LOS, b) NES with oblique LOS and c) GRS with perpendicular LOS. The same orbit-space grid points, FI- and bulk distributions were used as those in Figure 3.

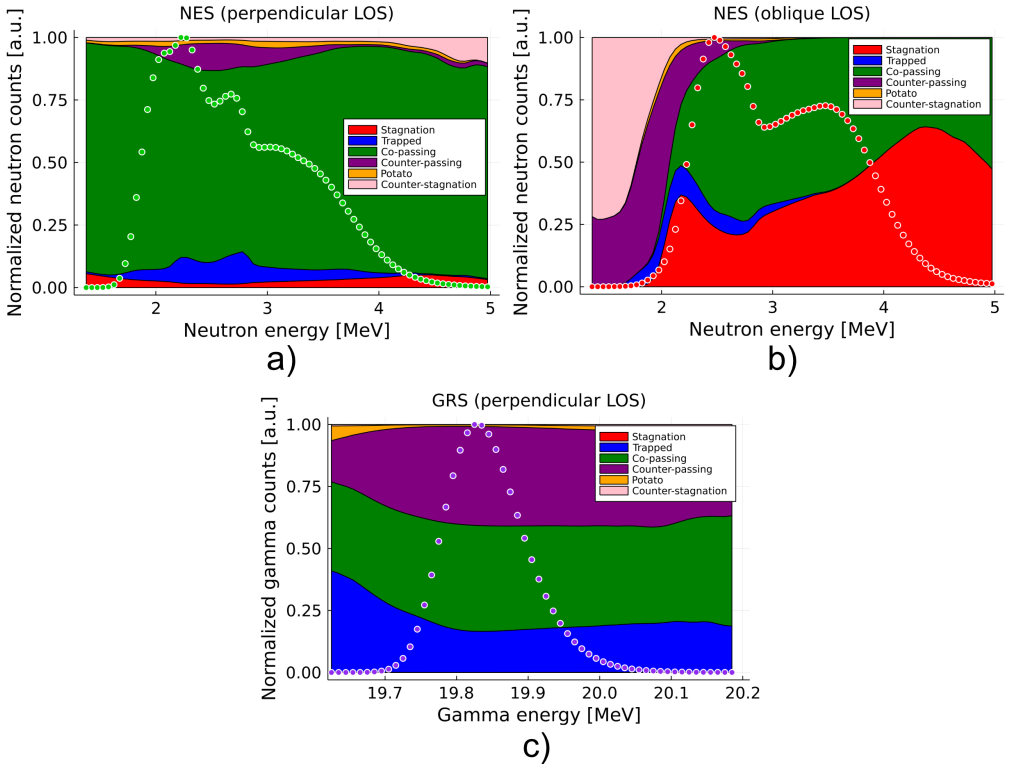

Figure 11. Same as Figure 10, but the sum of the orbit constituents has been normalized to 1.0 for all diagnostic energies of interest. The normalized 'WF' signals taken from Figure 3 have been superimposed for convenience.

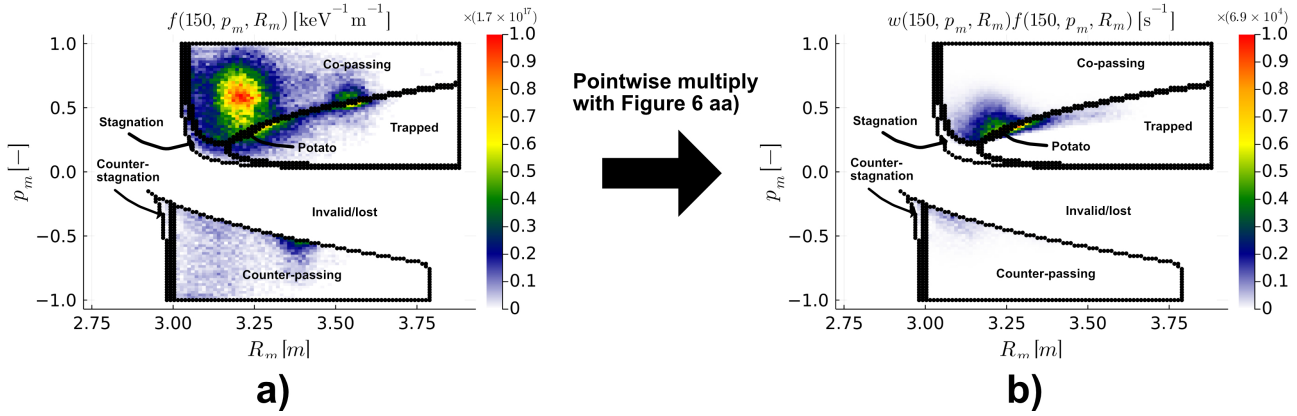

Figure 12. a) An orbit-space energy slice of the average FI deuterium distribution function for JET shot No. 94701 for our time window of interest. b) The data in panel a) is pointwise multiplied with the NES orbit weight function $w(150, p_\mathrm{m}, R_\mathrm{m})$ for the neutron energy $E_\mathrm{d} = 3$ MeV, corresponding to the weight function slice in Figure 6 aa).

perpendicular and an oblique LOS with NES and GRS diagnostics as examples. The orbit weight functions have been examined for different diagnostic- and FI-energies for the first time. Sensitivity patterns can be identified and understood via slice-by-slice examination in terms of FI energy, while superimposing the topological boundaries between different orbit types.

For the perpendicular LOS and the D(D,n)^{3}He reaction, at relatively low FI energies the sensitivity is highest for potato and counter-stagnation orbits. At increasingly high FI energies, the area of highest sensitivity tends toward the $p_\mathrm{m} = \pm 1.0$ boundaries, corresponding to co- and counter-passing orbits with ion pitch $(v_{||}/v)$ values close to 1.0. Orbit weight functions for increasingly high neutron energies have 3D patterns that remain qualitatively similar but are shifted 'upward' to increasingly high FI energies. The results can be used to conclude that TOFOR [36] (and any diagnostic sharing the LOS) is in general sensitive to neutrons originating from fast ions on potato orbits but not sensitive at all to neutrons originating from fast ions on stagnation orbits. This is because stagnation orbits at JET are mostly localized outside the viewing cone of TOFOR.

For the perpendicular LOS and the T(p,γ)^{4}He reaction, the orbit sensitivity is generally low for gamma energies below the gamma nominal birth energy and is concentrated to potato-like and counter-passing orbits localized near the magnetic axis. At the nominal birth energy, the weights are non-zero down to thermal energies where the sensitivity decreases as R_m increases. At $E \approx 50$ keV, the sensitivity is relatively high for orbits localized close to the magnetic axis with $p_\mathrm{m} \to \pm 1.0$. At increasingly high FI energies, the area of highest sensitivity tends towards potato-like and counter-stagnation orbits, before all weights become zero for sufficiently high FI energies.

For the oblique LOS and the D(D,n)^{3}He reaction, the areas of highest orbit sensitivity correspond to co-passing and stagnation orbits. The sensitivity is almost exclusively zero for counter-passing and counter-stagnation orbits since ions on those orbits are unable to produce the upshift required for the neutron energies of interest ($E_\mathrm{d} > 2.5$ MeV).

For all diagnostics, the orbit sensitivity is mostly determined by the location and orientation of the sightline (perpendicular, oblique, co-current, counter-current, poloidal projection etc.). For a given FI distribution function, the synthetic signals computed via the orbit weight functions are shown to closely match those computed with established forward models (in this work, the DRESS code [47] was used). In addition, the weight function signals can be split into their orbit-type constituents, which makes it possible to deduce signal origin in terms of orbit types. For JET shot No. 94701 and the time window of interest, the synthetic NES signals (corresponding to signals detectable by e.g. TOFOR [36] and the NE213-scintillator [39] but without an instrumental response function) are found to originate mostly from co-passing orbits. In addition, for the oblique LOS NES signal (e.g. the NE213-scintillator), a significant fraction originates from stagnation orbits.

In future work, orbit weight functions will be developed for two-step fusion reactions as well, which will enable us to express the sensitivities of diagnostics using e.g. alpha-particle FI orbits. In addition, orbit weight functions will be used to optimise the design of existing and new fast-ion diagnostics via, for example, maximising the amount of non-zero weights in orbit space. Finally, orbit weight functions will be used to reconstruct the full (E, p, R, z) FI distribution function from fusion-product measurements via orbit tomography as was recently achieved for FIDA measurements [31].

This is expected to help illuminate key relationships between the behavior of fast ions (including alpha particles) and various plasma instabilities such as Alfvén eigenmodes, sawteeth and energetic particle modes, causing undesired redistribution of fast ions. This is highly relevant both for ongoing experiments such as JET and future tokamaks such as ITER where fast ions will be crucial to achieve self-sustained heating of burning plasmas.

Acknowledgements

This work has received support from the Niels Bohr Foundation which is a merger of The Niels Bohr Grant, The Emil Herborg Grantpart, The Grant of MA Marcus Lorenzen, The Ole Rømer Foundation and The Julie Marie Vinter Hansen Travel Grant. The views and opinions expressed herein do not necessarily reflect those of The Royal Danish Academy of Sciences and Letters.

This work has been carried out within the framework of the EUROfusion Consortium, funded by the European Union via the Euratom Research and Training Programme (Grant Agreement No 101052200 — EUROfusion). Views and opinions expressed are however those of the author(s) only and do not necessarily reflect those of the European Union or the European Commission. Neither the European Union nor the European Commission can be held responsible for them.

References

[1] J Mailloux *et al* 2022 Nucl. Fusion in press
[2] D Moseev *et al* 2018 Rev. Mod. Plasma Phys. **2** 7
[3] W W Heidbrink and R B White 2020 Phys. Plasmas **27** 030901
[4] NN Gorelenkov *et al* 2003 Nucl. Fusion **43** 594
[5] SD Pinches *et al* 2006 Nucl. Fusion **46** S904–S910
[6] A Fasoli *et al* 2007 Nucl. Fusion **47** S264–S284
[7] R Ding *et al* 2015 Nucl. Fusion **55** 023013
[8] M Salewski March 2019 Fast-ion diagnostic in fusion plasmas by velocity-space tomography (Kongens Lyngby, Denmark: Technical University of Denmark)
[9] J Eriksson *et al* 2015 Nuclear Fusion **55** 123026
[10] M Salewski *et al* 2019 Journal of Instrumentation **14** C05019
[11] M Salewski *et al* 2012 Nucl. Fusion **52** 103008
[12] M Salewski *et al* 2013 Nucl. Fusion **53** 063019
[13] M Salewski *et al* 2014 Nucl. Fusion **54** 023005
[14] AS Jacobsen *et al* 2016 Plasma Phys. Control. Fusion **58** 045016
[15] M Salewski *et al* 2016 Nucl. Fusion **56** 106024
[16] M Salewski *et al* 2017 Nucl. Fusion **57** 056001
[17] M Salewski *et al* 2018 Nucl. Fusion **58** 096019
[18] M Salewski *et al* 2018 Fusion Science and Technology **74** 23–36
[19] W W Heidbrink *et al* 2007 Plasma Phys. Control. Fusion **49** 1457–1475
[20] M Salewski *et al* 2014 Plasma Phys. Control. Fusion **56** 105005
[21] M Salewski *et al* 2011 Nuclear Fusion **51** 083014
[22] M Salewski *et al* 2016 Nucl. Fusion **56** 046009
[23] M Salewski *et al* 2015 Nucl. Fusion **55** 093029
[24] J Galdon-Quiroga *et al* 2018 Plasma Phys. Control. Fusion **60** 105005
[25] WW Heidbrink *et al* 2021 Plasma Phys. Control. Fusion **63** 055008
[26] M Salewski *et al* 2018 Fusion Science and Technology **74** 23–36
[27] A S Jacobsen *et al* 2015 Nucl. Fusion **55** 053013
[28] A S Jacobsen *et al* 2017 Rev. Sci. Instrum. **88** 073506
[29] B S Schmidt *et al* 2021 Rev. Sci. Instrum. **92** 053528
[30] WW Heidbrink and GJ Sadler 1994 Nucl. Fusion **43** 535
[31] L Stagner *et al* 2022 Nucl. Fusion **62** 026033
[32] Stagner L and Heidbrink W W 2017 Physics of Plasmas **24** 092505
[33] H Järleblad *et al* 2021 Rev. Sci. Instrum. **92** 043526
[34] J Eriksson *et al* 2019 Plasma Phys. Control. Fusion **61** 014027
[35] M Nocente *et al* 2020 Nucl. Fusion **60** 124006
[36] M Gatu Johnson *et al* 2008 Nucl. Instrum. Methods Phys. Res. A **591** 417–430
[37] M Nocente *et al* 2010 Rev. Sci. Instrum. **81** 10D321
[38] M Nocente *et al* 2021 Rev. Sci. Instrum. **92** 043537
[39] F Binda *et al* 2014 Rev. Sci. Instrum. **85** 11E23
[40] JA Rome and YK M Peng 1979 Nucl. Fusion **19** 1193
[41] Y Kazakov *et al* 2021 Phys. of Plasmas **28** 020501
[42] Ž Štancar *et al* 2021 Nucl. Fusion **61** 126030
[43] Y Kazakov *et al* 2020 Nucl. Fusion **60** 112013
[44] M Kikuchi, K Lackner & MQ Tran 2012 Fusion Physics (Vienna, Austria: International Atomic Energy Agency)
[45] Stagner L 2018 Inference of the Fast-ion Distribution Function Ph.D. thesis University of California, Irvine
[46] A Bierwage *et al* 2021 *Representation and modeling of charged particle distributions in tokamaks* arXiv arXiv:2111.08224v1 [physics.plasm-ph]
[47] J Eriksson *et al* 2016 CPC **199** 40–46
[48] Breslau J, Gorelenkova M, Poli F, Sachdev J, Pankin A and Perumpilly G 2018 Transp [Computer Software] `https://doi.org/10.11578/dc.20180627.4`
[49] A Pankin, D McCune, R Andre *et al* 2004 CPC **159,3** 157–184
[50] Brambilla M 1999 Plasma Phys. Cont. Fusion **41** 1
[51] Jae-Min Kwon *et al* 2006 Development of xgc-rf for global guiding-center particle simulation of minority icrh heated plasmas in a general tokmak geometry 48th Annual Meeting of the Division of Plasma Physics URL `http://meetings.aps.org/link/BAPS.2006.DPP.VP1.115`
[52] Jae-Min Kwon Douglas McCune C C 2007 Enhancement of nubeam for the simulation of fast ion and rf-wave interaction based on the quasi-linear theory 49th Annual Meeting of the Division of Plasma Physics vol 52 URL `http://meetings.aps.org/link/BAPS.2007.DPP.UP8.83`
[53] M Dreval *et al* 2022 Nucl. Fusion in press
[54] M Nocente *et al* 2015 Nucl. Fusion **55** 123009